forum acusticum 2026
8-12 September · Graz, Austria

EXPERIMENTAL AND NUMERICAL INVESTIGATION OF ACOUSTIC SCATTERING USING BOOSTLETS

Augusto Fantinelli[1], Annika Strömhäll[2], U. Peter Svensson[3], Marc Arnela[1], Elias Zea[2]

[1] *Human-Environment Research (HER), La Salle, Universitat Ramon Llull, Catalonia, Spain*
[2] *The Marcus Wallenberg Laboratory for Sound and Vibration Research, Department of Engineering Mechanics, KTH Royal Institute of Technology, Stockholm, Sweden*
[3] *Acoustics group, Department of Electronic Systems, Norwegian University of Science and Technology, Trondheim, Norway*

Abstract

Modelling the interaction of sound waves with objects and surfaces is challenging due to the complex space–time behaviour of acoustic fields. In practice, surface roughness and finite object dimensions cause sound reflections to deviate from ideal specular behaviour, producing scattered and diffracted fields. While separating the total sound field into incident, reflected, scattered, and diffracted components is conceptually appealing, achieving it from spatial measurements remains a non-trivial problem. This work applies boostlet decompositions to simultaneously separate and analyse these components using a 1D line microphone array near the scatterer. The core idea is that each wave results from geometrically thresholding boostlet decompositions. The method is applied to a benchmark problem in which a spherical wave impinges on a circular disk of radius 40 cm. Measurements are performed in an anechoic chamber using a 6-DOF robotic arm mounted on a linear track, sampling the acoustic pressure along the axis and in front of the disk. Numerical predictions are obtained using an edge-diffraction-based method that separates the time-domain solution into geometrical-acoustics and diffraction components. The reconstructed direct, specular, and edge-diffracted fields are validated against these components and compared with the experiment, and estimating a scattering coefficient is left for future work.

Keywords: *sound scattering, wavefields, boostlets, spatial sound-field sampling*

Corresponding author: *marc.arnela@salle.url.edu.*

1. Introduction

Acoustic surface scattering is standardized in ISO 17497: Part 1 defines the random-incidence scattering coefficient in a reverberation room, whereas Part 2 characterizes directional diffusion in the free field [1], [2]. For finite objects, measurements contain direct, specularly reflected, and edge-diffracted wavefronts that may overlap in space, time, and frequency. Edge diffraction contributes to the non-specular field and can therefore bias interpretations based on an idealized infinite surface [3], [4]. A common separation procedure subtracts a free-field measurement from the total response and time-windows the residual [5], [6]. However, subtraction is sensitive to gain and sub-sample delay differences, while point-wise temporal windows reduce low-frequency resolution when the arrivals overlap.

Spatial inverse methods reduce the reliance on temporal processing. Richard et al. reconstructed the scattering of a finite specimen from near-field pressure and particle-velocity measurements [7]. Brandão and Fernandez-Grande investigated edge-diffraction bias in pressure-array measurements and used wavenumber-domain inversion to identify specular and diffracted contributions above finite absorbers [8], [9]. More recently, Brandão et al. separated incident and scattered fields near full-size rigid diffusers using regularized near-field holography [10]. These studies show the value of spatial sampling, but their results depend on the measurement aperture and variables, regularization, and propagation model.

Boostlets provide a complementary representation built from space–time atoms whose dilation and hyperbolic-rotation parameters follow the dispersion geometry of the nondispersive wave equation [11], [12]. Propagating wavefronts can therefore concentrate in a small set of scale–boost–translation maps, enabling phase fronts with different geometries to occupy

different regions of the Fourier plane. This localization makes boostlets suitable for separating non-trivially overlapping wavefield components.
In this work, we investigate the acoustic scattering at a line of receivers between a monopole-like source and a circular disk of radius 0.4 m. The measured field is compared with a time-domain edge-diffraction simulation of the same geometry. For a blind test, the simulated direct, geometrical-reflection, and diffraction components are summed before processing. The objective is to reconstruct the direct, specular, and edge-diffracted fields without a separate free-field subtraction.
This work is organised as follows. Section 2 presents the experimental setup, the numerical simulation, and the boostlet signal analysis. Section 3 displays the results of the boostlet application on the measured and simulated data, the performed thresholding, and the reconstructed sound fields for both cases. Section 4 concludes the discussion.

2. Methodology

2.1. Experimental procedure

Measurements were performed in the anechoic chamber of La Salle - Universitat Ramon Llull, using a GRAS 46BF-1 1/4" free-field microphone mounted in a 6-DOF placed on a linear track [13]. An acrylic disk with an 80 cm diameter and 8 mm thickness was placed 2 m away from the sound source, a SEAS 25TFFN/G (H0615) with a diaphragm diameter of 26 mm. This speaker is very nearly omnidirectional within the angular sector occupied by the scattering disk, with some directivity towards higher frequencies. Impulse responses were measured in 313 positions starting 40 cm from the source and ending 2 cm from the disk, with a spacing of 0.5 cm. Figure 1 displays the described assembly.
Exponential sine sweeps from 80 Hz to 12 kHz with a duration of 1 s were used to measure the impulse responses. Linear fade-in from 20 Hz to 80 Hz and fade-out from 12 kHz to 14 kHz were applied to avoid pre-ringing artefacts [14]. The time-analysis window is set to 670 samples, starting slightly before the direct wave hits the array. The emitted signals were acquired using a Type 3160-A-022 Brüel & Kjaer LANXI module with a UA-3102-041 front end, using a sampling frequency of 131072 Hz. The signals were amplified using an Ecler XPA3000 amplifier with gain to achieve a peak voltage of 0.8 V at the loudspeaker.

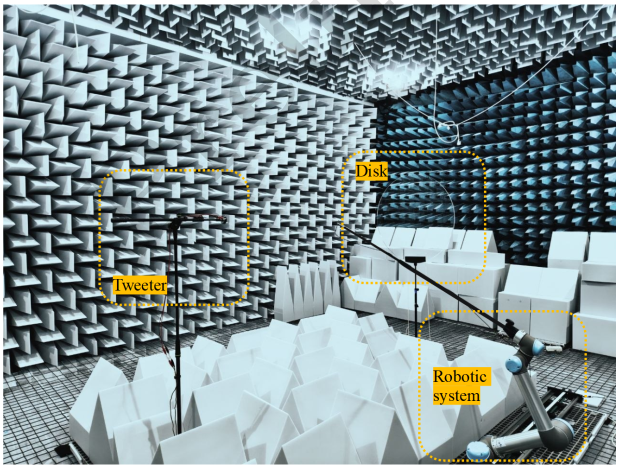

Figure 1: Experimental setup displaying the speaker, the disk, and the automated robotic system.

2.2. Numerical simulations

A numerical simulation of the experiment was performed using the `Edge Diffraction Toolbox` [15] in MATLAB, retaining its separate direct, geometrical-reflection, and edge-diffraction responses [16]. The disk is modeled as an equal-area 8-sided thin polygon with first-order edge diffraction. The centre of the polygon was displaced laterally by 30 mm relative to the source-microphone axis, while its plane remained perpendicular to that axis. This empirical offset was introduced in the original numerical model because it improved agreement with the measurements.
Each component was convolved with the first 256 samples of a fitted tweeter response: a second-order high pass, a 12th-order IIR equalizer, and an order-250 FIR low pass at 12.4 kHz. Measurement and model are normalized to unit transfer-function magnitude at 6 kHz and 1 m. Their respective 5- and 125-sample delays at 131072 Hz were removed before resampling, with no additional simulation gain. All 393 fitted receiver positions were simulated, and the analysis uses the final 313, beginning at 0.422 m, as in the measurement.

2.3. Boostlet signal analysis

Let $\boldsymbol{\zeta} = (x, ct)^\mathsf{T}$ be a dimensionally homogeneous space–time coordinate, where c is the speed of sound. Given a mother function $\psi \in L^2(\mathbb{R}^2)$, a continuous boostlet is [11]

$$\begin{aligned} \psi_\mu(\boldsymbol{\zeta}) &= a^{-1}\psi\left(\Lambda_\theta^{-1}\frac{\boldsymbol{\zeta}-\boldsymbol{\tau}}{a}\right), \\ \Lambda_\theta &= \begin{bmatrix} \cosh\theta & -\sinh\theta \\ -\sinh\theta & \cosh\theta \end{bmatrix}, \end{aligned} \tag{1}$$

where the multi-index $\mu = \{a, \theta, \boldsymbol{\tau}\}$ includes a dilation $a > 0$, a Lorentz boost $\theta \in \mathbb{R}$, and translations across 1+1D space–time $\boldsymbol{\tau} = (\tau_x, c\tau_t)^\mathsf{T}$. Defining the space–time Fourier transform of the sound pressure signal $p(\boldsymbol{\zeta}) \in L(\mathbb{R}^2)$ with $\widehat{p}(\boldsymbol{\xi}) = \widehat{p}(k,\omega) = \iint p(x,t)\exp[-\mathrm{i}(kx-\omega t)]\,\mathrm{d}x\,\mathrm{d}t$, the Fourier spectrum of the mother boostlet in (1) becomes $\widehat{\psi}_\mu(\boldsymbol{\xi}) = a\,\exp(-2\pi\mathrm{i}\boldsymbol{\tau}^\mathsf{T}\boldsymbol{\xi})\hat{\psi}(M_{a,\theta}^\mathsf{T}\boldsymbol{\xi})$. From now on, we shall use the operators $\mathcal{F}$ and $\mathcal{F}^{-1}$ to denote the forward and inverse fast Fourier transforms.
Physically speaking, the dilation selects a hyperbolic frequency interval, the boost selects the wave phase speed, and translations localize the phase front. The regions $|\omega| < c|k|$ and $|\omega| > c|k|$ are referred to as the near- and far-field radiation cones. As discussed in [11],

boostlets cannot be defined on the radiation cone $|\omega| = c|k|$, for which a scaling function, $\phi_{\boldsymbol{\tau}} \in L(\mathbb{R}^2)$, must be introduced. The complete boostlet dictionary is thus composed of the scaling function $\phi_{\boldsymbol{\tau}}(\boldsymbol{\zeta})$ and the boostlet functions $\psi_\mu(\boldsymbol{\zeta})$.

2.3.1. Sampling the boostlet dictionary

The measured pressure matrix and the source-filtered numerical components are delay-corrected and resampled in time to $f_{\mathrm{r}} = c/\Delta x \approx 67.89$ kHz, so that one temporal sample represents propagation over one nominal spatial increment. The analysis uses $\Delta x = 5$ mm and $c = 339.45$ m/s, anchoring the uniform FFT grid at the fitted first retained position (0.422 m). Both coordinate ends are then zero-padded by 200 samples to reduce periodicity effects.

The discrete dictionary follows the tensor Meyer-wavelet construction in [11], with four dyadic dilation levels and eighteen boost levels. Near-field boostlets are removed from the dictionary and are out of the scope of this work. Additionally, the boostlet scaling function is smoothly partitioned into propagating along the $+x$ axis, $\phi_+(\boldsymbol{\zeta})$, and the $-x$ axis, $\phi_-(\boldsymbol{\zeta})$. This gives 74 dictionary atoms: two scaling functions and 72 far-field boostlets.

2.3.2. Energetic thresholding

The coefficient maps of the two scaling functions and the μ-th boostlet function are obtained via

$$\begin{aligned} s_+(\boldsymbol{\tau}) &= \mathcal{F}^{-1}\left\{\widehat{s}_+(\boldsymbol{\xi})\right\} = \mathcal{F}^{-1}\left\{\widehat{p}(\boldsymbol{\xi})\overline{\widehat{\phi}_+(\boldsymbol{\xi})}\right\}(\boldsymbol{\tau}) \\ s_-(\boldsymbol{\tau}) &= \mathcal{F}^{-1}\left\{\widehat{s}_-(\boldsymbol{\xi})\right\} = \mathcal{F}^{-1}\left\{\widehat{p}(\boldsymbol{\xi})\overline{\widehat{\phi}_-(\boldsymbol{\xi})}\right\}(\boldsymbol{\tau}) \\ b_\mu(\boldsymbol{\tau}) &= \mathcal{F}^{-1}\left\{\widehat{b}_\mu(\boldsymbol{\xi})\right\} = \mathcal{F}^{-1}\left\{\widehat{p}(\boldsymbol{\xi})\overline{\widehat{\psi}_\mu(\boldsymbol{\xi})}\right\}(\boldsymbol{\tau}) \end{aligned} \tag{2}$$

The two scaling maps are always retained and processed separately according to their propagation direction along the array. The remaining boostlet maps are retained in a two-fold thresholding (denoising) operation. First, boostlets whose matrix-norm energy $\|b_\mu\|_2^2$ exceeds the threshold

$$r_{\mathrm{th}} = \mathrm{mean}_\mu\left(\|b_\mu\|_2^2\right) - 0.5\,\mathrm{std}_\mu\left(\|b_\mu\|_2^2\right) \tag{3}$$

survive, yielding the strongest scale–boost maps. Second, we compute the cross-correlation $\rho_\mu(\boldsymbol{\tau}) = \langle b_\mu, \psi_\mu\rangle(\boldsymbol{\tau})$ for each retained boostlet map μ, and further threshold its translation coefficients. Mathematically, the thresholding reads

$$\widetilde{b}_\mu(\boldsymbol{\tau}) = \begin{cases} b_\mu(\boldsymbol{\tau}), & \mu \in \widetilde{\mu}, \\ 0, & \text{otherwise}, \end{cases} \tag{4}$$

where $\widetilde{\mu} = \left\{\mu : \|b_\mu\|_2^2 > r_{\mathrm{th}}, |\rho_\mu(\boldsymbol{\tau})| > 0.01\|\rho_\mu\|_\infty\right\}$.

2.3.3. Joint wavefront separation

The causal partition separates the direct wave from reflection and edge diffraction, which are captured by translations after the source wave reaches the disk: $\Pi_{\mathrm{dir}}(\boldsymbol{\tau}) = \mathbb{1}[\tau_t \le \tau_{\mathrm{D}}]$, where $\tau_{\mathrm{D}} = (d_{\mathrm{D}} + 40\ \mathrm{mm})/c \approx 6.01$ ms, corresponding to the source-disk travel time. For disk radius R, the specular and first edge-diffracted arrivals at translation τ_x are $\tau_{\mathrm{spec}}(\tau_x) = (2d_{\mathrm{D}} - \tau_x)/c$ and $\tau_{\mathrm{diff}}(\tau_x) = (\sqrt{d_{\mathrm{D}}^2 + R^2} + \sqrt{(d_{\mathrm{D}} - \tau_x)^2 + R^2})/c$. We use these arrival times to separate specular and diffracted boostlets with two masks that partition their translation coefficients:

$$\begin{aligned} \Pi_{\mathrm{spec}}(\boldsymbol{\tau}) &= \mathbb{1}\left[\tau_t \le (\tau_{\mathrm{spec}}(\tau_x) + \tau_{\mathrm{diff}}(\tau_x))/2\right], \\ \Pi_{\mathrm{diff}}(\boldsymbol{\tau}) &= 1 - \Pi_{\mathrm{spec}}(\boldsymbol{\tau}). \end{aligned} \tag{5}$$

The translation midpoint is a geometry-informed heuristic that uses a centred-disk approximation. A complementary raised-cosine partition around d_{D}/c finally redistributes direct/specular leakage while preserving their sum.

Finally, the separated direct, specular, and diffracted fields are reconstructed via

$$\begin{aligned} p^\star_{\mathrm{dir}}(\boldsymbol{\zeta}) = {} & \mathcal{F}^{-1}\left\{\mathcal{F}\{\Pi_{\mathrm{dir}} s_+\}\overline{\widehat{\phi}_+}\right\} + \\ & \mathcal{F}^{-1}\left\{\sum_{\mu\in\tilde{\mu}} \mathcal{F}\{\Pi_{\mathrm{dir}}\widetilde{b}_\mu\}\overline{\widehat{\psi}_\mu}\right\}, \\ p^\star_{\mathrm{spec}}(\boldsymbol{\zeta}) = {} & \mathcal{F}^{-1}\left\{\mathcal{F}\left\{\Pi_{\mathrm{spec}} s_-\right\}\overline{\widehat{\phi}_-}\right\} + \\ & \mathcal{F}^{-1}\left\{\sum_{\mu\in\tilde{\mu}} \mathcal{F}\{\Pi_{\mathrm{spec}}\widetilde{b}_\mu\}\overline{\widehat{\psi}_\mu}\right\}, \\ p^\star_{\mathrm{diff}}(\boldsymbol{\zeta}) = {} & \mathcal{F}^{-1}\left\{\mathcal{F}\left\{\Pi_{\mathrm{diff}} s_-\right\}\overline{\widehat{\phi}_-}\right\} + \\ & \mathcal{F}^{-1}\left\{\sum_{\mu\in\tilde{\mu}} \mathcal{F}\left\{\Pi_{\mathrm{diff}}\widetilde{b}_\mu\right\}\overline{\widehat{\psi}_\mu}\right\}, \end{aligned} \tag{6}$$

and the total field can be reconstructed by $p^\star_{\mathrm{tot}}(\boldsymbol{\zeta}) = p^\star_{\mathrm{dir}}(\boldsymbol{\zeta}) + p^\star_{\mathrm{spec}}(\boldsymbol{\zeta}) + p^\star_{\mathrm{diff}}(\boldsymbol{\zeta})$.

3. Results

3.1. Sound field thresholding and reconstruction

Figure 2 compares the measured and reconstructed fields in space–time and Fourier space, and gives the scores of all 74 dictionary maps. The two scaling channels have the largest scores, consistent with direct and specular energy concentrating near the acoustic radiation cone. The remaining scores form four dilation clusters and are strongest at dilations 3–4 (which correspond to the lower-frequency range in the Fourier spectra). Here $r_{\mathrm{th}} = 1.05 \times 10^{-4}$, equivalent to a matrix-norm threshold of 0.0103, and 45 coefficient maps survive, including the scaling maps. Their synthesis preserves the direct, reflected, and curved diffracted fronts.

Figure 3 presents the simulation and reconstruction

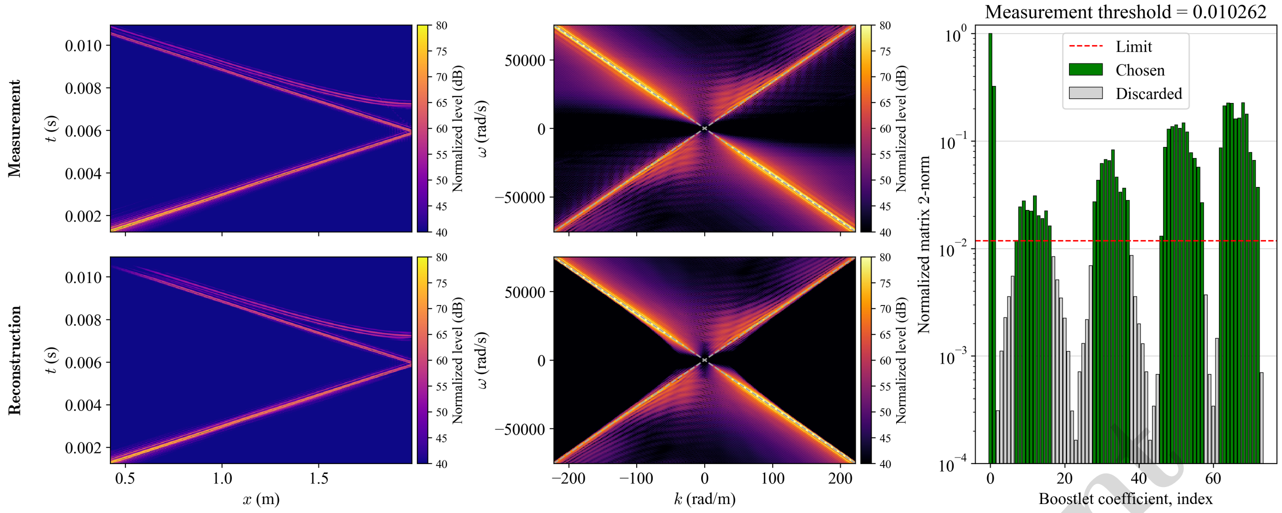

Figure 2: Measured field (top), boostlet reconstruction (bottom), and normalized matrix spectral-norm scores (right). The Fourier panels (center) show the acoustic radiation cone $|\omega| = c|k|$ (grey dashed).

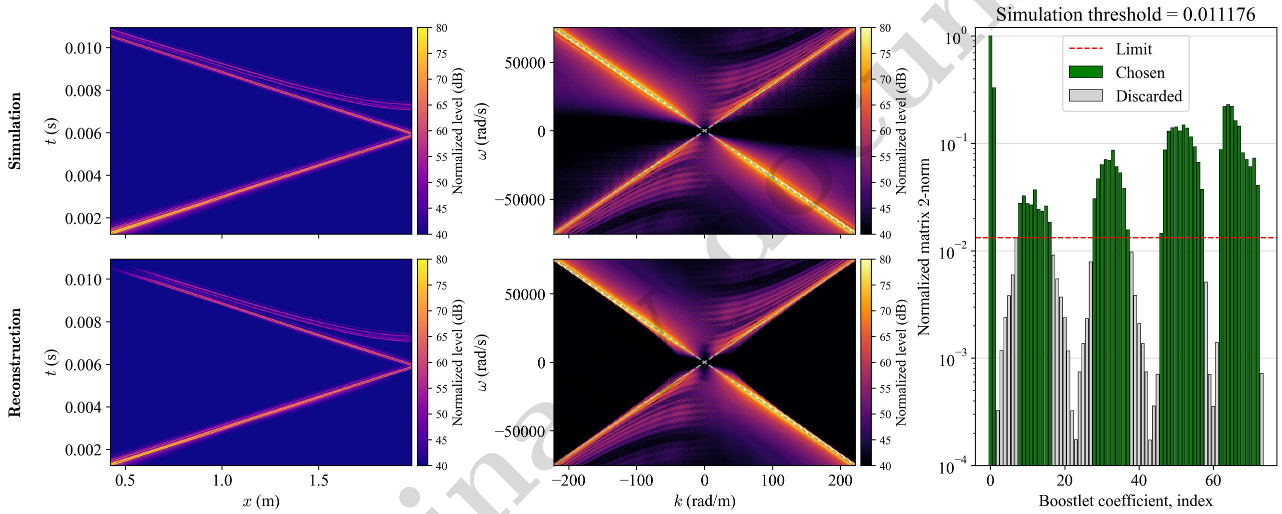

Figure 3: Simulation (top), boostlet reconstruction (bottom), and normalized matrix spectral-norm scores (right).

using the notation of Fig. 2. Its direct and specular fronts closely match their measured counterparts. The same four coefficient clusters are recovered, and $r_{\mathrm{th}} = 1.25 \times 10^{-4}$ (norm-equivalent 0.0112) retains 44 coefficient maps including the two scaling maps.

Overall, the simulated fields and their reconstructions, as well as the corresponding energy plots, reproduce well the experimental counterparts in Fig. 2. Two important distinctions can be observed. First, the measured hyperbolic content away from the radiation cone $|\omega| = c|k|$ seems to decay more smoothly than that in the simulation, which contains a hyperbolic notch with apex around $2 \cdot 10^4$ rad/s. Second, the boostlet coefficient map $\mu = 5$ (7 in the abscissa), which survives the threshold obtained with experimental data but not with simulated data.

3.2. Sound field separation

Figures 4 and 5 compare the direct, specular, and edge-diffracted fields reconstructed from the total measured and simulated fields. The decomposition recovers the oppositely inclined direct and specular fronts and the curved diffracted front. The normalized correlations with the corresponding individually simulated references, listed as direct, specular, and diffracted, are $(0.973, 0.950, 0.561)$ for the measurement and $(0.981, 0.957, 0.937)$ for the simulation. Correlations with non-corresponding reference components remain below 0.015, indicating little cross-assignment between the three fields. The lower measured diffraction correlation reflects differences in the detailed space–time distribution of the weaker diffracted field, particularly where it approaches the specular front asymptotically.

In Fourier space, the direct and specular spectra

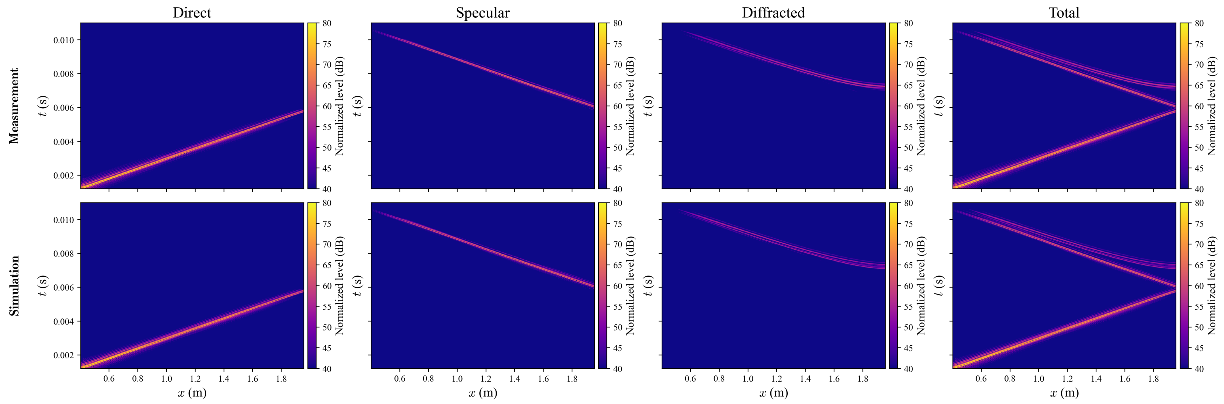

Figure 4: Three-field reconstruction in space–time for the measurement (top) and simulation (bottom): direct (left), specular (mid-left), edge-diffracted (mid-right). The total fields (right) are included for comparison and correspond to the bottom-left panels of Figs. 2 and 3.

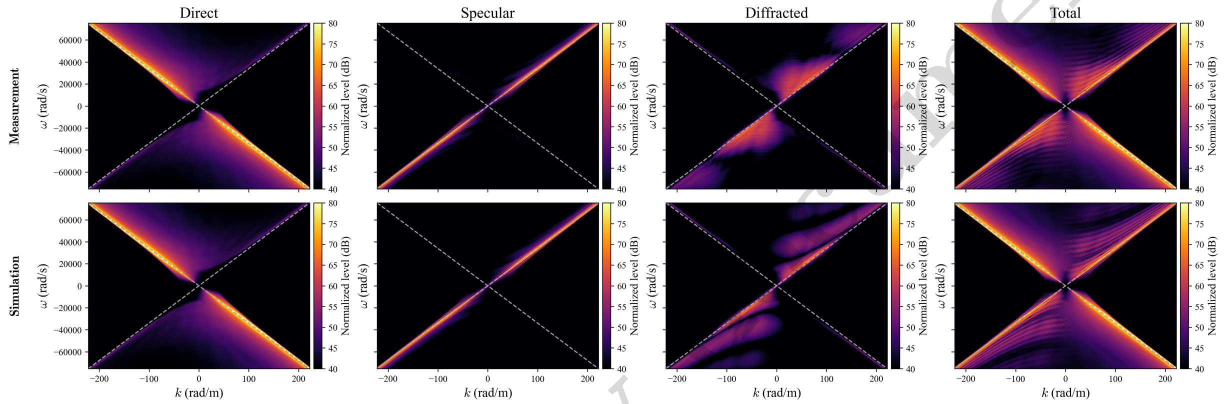

Figure 5: Wavenumber–frequency counterparts of Fig. 4. Dashed lines denote the radiation-cone boundary $|\omega| = c|k|$.

concentrate near opposite sides of the radiation cone and are represented primarily by their corresponding scaling channels. The opposite slopes reflect their opposite propagation directions along the array. The hyperbolic portion of the diffracted field occupies boostlet coefficients away from the cone, whereas its asymptotic portion approaches the specular field and overlaps the reflected scaling channel. The separation therefore combines localization by the boostlet dictionary with a geometry-informed partition in translation space, with the greatest uncertainty occurring in this overlap region.

Small differences remain between the measured and simulated diffraction spectra. In particular, the diffraction-associated hyperbolic ridges are broader and less sharply defined in the measurement. This broadening may reflect the source's frequency- and angle-dependent radiation, differences between the physical and idealized disk geometries, and uncertainties in the microphone positions and source-disk-array alignment. Additional scattering from secondary structures, including the microphone holder, positioning robot, and disk support, may also introduce components that are absent from the numerical model.

Overall, the findings in this work support the simultaneous wavefront separation by applying boostlet-thresholding to line-microphone array data.

4. Conclusions

This work investigated acoustic scattering by a disk using measured and simulated sound fields sampled along a line array oriented orthogonally to the source–disk axis, without requiring free-field subtraction. The boostlet decomposition separated the total field into direct, specular, and edge-diffracted components through coefficient selection and a geometry-informed boundary in the boostlet translation space. The separated simulated fields closely agree with the corresponding individually simulated components, while the largest discrepancy occurs for the measured diffracted field.

The main takeaway message is two-fold: (i) the direct and specular components is composed of broadband functions propagating with grazing incidence on the array, captured naturally by boostlet scaling coefficients; and (ii) the diffracted component is composed of broadband hyperbolic patterns, captured by boostlet coefficients.

Future work will develop robust, data-driven estimates of the thresholds and separation boundaries under noisy conditions, extend the analysis to off-axis measurements, and use the separated fields to estimate scattering coefficients.

5. Acknowledgments

This publication is part of the project CharPAL PID2025-175028NB-I00 funded by MICIU/AEI/10.13039/501100011033 and by ERDF, EU, and supported by the Swedish Research Council (Vetenskapsrådet) Grants No. 2020-04668 and 2025-03936. The first and fourth authors thank the Catalan Government (Departament de Recerca i Universitats) for the grant 2021 SGR 01396 awarded to the HER group.

References

[1] International Organization for Standardization, *Acoustics—sound-scattering properties of surfaces—part 1: Measurement of the random-incidence scattering coefficient in a reverberation room*, Geneva, Switzerland, 2004. [Online]. Available: `https://www.iso.org/standard/31397.html`.

[2] International Organization for Standardization, *Acoustics—sound-scattering properties of surfaces—part 2: Measurement of the directional diffusion coefficient in a free field*, Geneva, Switzerland, 2012. [Online]. Available: `https://www.iso.org/standard/55293.html`.

[3] U. P. Svensson, R. I. Fred, and J. Vanderkooy, "An analytic secondary source model of edge diffraction impulse responses," *The Journal of the Acoustical Society of America*, vol. 106, no. 5, pp. 2331–2344, 1999. DOI: `10.1121/1.428071`.

[4] E. Brandão, A. Lenzi, and J. Cordioli, "Estimation and minimization of errors caused by sample size effect in the measurement of the normal absorption coefficient of a locally reactive surface," *Applied Acoustics*, vol. 73, no. 6–7, pp. 543–556, 2012. DOI: `10.1016/j.apacoust.2011.09.010`.

[5] E. Mommertz, "Angle-dependent in-situ measurements of reflection coefficients using a subtraction technique," *Applied Acoustics*, vol. 46, no. 3, pp. 251–263, 1995. DOI: `10.1016/0003-682X(95)00027-7`.

[6] P. Robinson and N. Xiang, "On the subtraction method for in-situ reflection and diffusion coefficient measurements," *The Journal of the Acoustical Society of America*, vol. 127, no. 3, EL99–EL104, 2010. DOI: `10.1121/1.3299064`.

[7] A. Richard, D. Fernández Comesãna, J. Brunskog, C. H. Jeong, and E. Fernandez-Grande, "Characterization of sound scattering using near-field pressure and particle velocity measurements," *The Journal of the Acoustical Society of America*, vol. 146, no. 4, pp. 2404–2414, 2019. DOI: `10.1121/1.5126942`.

[8] E. Brandão and E. Fernandez-Grande, "Influence of edge diffraction on the in situ measurement of impedance using microphone arrays," in *Proceedings of the 49th International Congress and Exposition on Noise Control Engineering, INTER-NOISE 2020*, Seoul, Republic of Korea, 2020.

[9] E. Brandão and E. Fernandez-Grande, "Analysis of the sound field above finite absorbers in the wave-number domain," *The Journal of the Acoustical Society of America*, vol. 151, no. 5, pp. 3019–3030, 2022. DOI: `10.1121/10.0010355`.

[10] E. Brandão, E. Fernandez-Grande, C. Gaudeoso, S. A. Verburg, and A. Richard, "Three-dimensional directivity measurement of acoustic diffusers using regularized holography and sound field separation," *The Journal of the Acoustical Society of America*, vol. 158, no. 5, pp. 3936–3948, 2025. DOI: `10.1121/10.0039893`.

[11] E. Zea, M. Laudato, and J. Andén, "A boostlet transform for wave-based acoustic signal processing in space–time," *Signal Processing*, vol. 244, p. 110 528, 2026. DOI: `10.1016/j.sigpro.2026.110528`.

[12] E. Zea, M. Laudato, and J. Andén, "Sparse wavefield reconstruction and denoising with boostlets," in *Proc. International Conference on Sampling Theory and Applications (SampTA)*, 2025. DOI: `10.1109/SampTA64769.2025.11133531`.

[13] A. Fantinelli, M. Arnela, E. Brandão, and E. Fernandez-Grande, "A robotic system for space-time characterization of parametric acoustic sound sources," in *Proc. of Forum Acusticum 2025*, European Acoustics Assosciation, Málaga, Spain, 2025.

[14] M. Arnela, C. Martínez-Suquía, and O. Guasch, "Characterization of an omnidirectional parametric loudspeaker with exponential sine sweeps," *Appl. Acoust.*, vol. 182, p. 108 268, 2021.

[15] U. P. Svensson, *Edge diffraction toolbox for matlab, v. 0.216 [computer program]*, , `https://github.com/upsvensson/Edge-diffraction-Matlab-toolbox.`. Last accessed 2026-07-27.

[16] S. U. Vikøren and U. P. Svensson, "Measured and computed reflection from a finite plate," in *Proc. of Euroregio and Baltic Nordic-Acoustic Meetings Joint Acoustics Conference*, 2022, pp. 1–10.